J Mater Sci: Mater Electron (2015) 26:8147–8159
DOI 10.1007/s10854-015-3475-4

# Preparation, structural and micromechanical properties of (Al/Mg) co-doped ZnO nanoparticles by sol–gel process

**E. Asikuzun[1] · O. Ozturk[1,2] · L. Arda[3] · D. Akcan[3] · S. D. Senol[4] · C. Terzioglu[5]**

Received: 6 March 2015 / Accepted: 8 July 2015 / Published online: 12 July 2015


**Abstract** $Zn_{0.90}Mg_{0.10-x}Al_xO$ (x = 0.0, 0.1, 0.2, 0.3, 0.4, 0.5 and 0.10) nanoparticles were prepared by using sol–gel technique. The effects of Al and Mg doping on the structural and mechanical properties were investigated by using X-Ray diffraction (XRD), scanning electron microscopy (SEM) and digital micro-hardness tester, respectively. The grain size, *a* and *c* lattice parameters and morphology of nanoparticles were characterized by XRD and SEM measurements. The grain sizes of Al/Mg co-doped ZnO nanoparticles were also calculated by Scherrer–Warren equation. *a* and *c* lattice parameters are calculated from XRD peaks. According to the results it was observed that the grain sizes increased with increasing the Al doping. *c* lattice parameter partially decreased with Al doping. The experimental results of hardness measurements were analyzed using Meyer's law, proportional specimen resistance model, elastic/plastic deformation model, and Hays–Kendall (HK) approach. It was observed that *HK* approach is the most successful model for the micro-hardness analysis of Al/Mg co-doped ZnO materials.

✉ E. Asikuzun
easikuzun@kastamonu.edu.tr

[1] Department of Physics, Faculty of Arts and Sciences, Kastamonu University, 37100 Kastamonu, Turkey

[2] Reseach and Application Center, Kastamonu University, 37100 Kastamonu, Turkey

[3] Department of Mechatronics Engineering, Faculty of Engineering and Natural Sciences, Bahcesehir University, 34349 Besiktas, Istanbul, Turkey

[4] Department of Chemistry, Faculty of Arts and Sciences, Abant Izzet Baysal University, 14280 Bolu, Turkey

[5] Department of Physics, Faculty of Arts and Sciences, Abant Izzet Baysal University, 14280 Bolu, Turkey

## 1 Introduction

Transparent conducting oxide (TCO), including both traditional n-type (IZO, ITO, doped ZnO, SnO and $In_2O_3$) and p-type ($CuAlO_2$ and $SrCu_2O_2$) materials has been used for several applications such as flat panel displays, low emissivity windows, sensors, and transparent electronics to improve applications [1–3].

Among traditional n-type (IZO, ITO, doped ZnO, SnO and $In_2O_3$) and p-type (CuAlO2 and $SrCu_2O_2$) materials, Indium tin oxide (ITO) has been widely used for transparent conducting oxide (TCO) material due to electrical conductivity and optical transparency, but it has some disadvantages (high cost, low stability and toxicity) [4, 5]. Therefore, recently doped ZnO have attracted extensive interest. This interest is resulted from high electrochemical stability, absence of toxicity, low cost as well good mechanical strength, and high direct band gap and a large exciton binding energy of 60 meV at room temperature [6]. The physical and chemical properties and applications of the ZnO are affected by the doping elements and concentration, and band gap modulation [7–10]. This strongly depends on the preparation method and condition. As a result, the ZnO was doped with elements (Al, Ga, In, Cu, Mg and so on) to increase electrical conductivity and transmittance in the visible range and stability against heat by using various methods such as magnetron DC sputtering, magnetron RF sputtering, metal organic chemical voper deposition (MOCVD), sol–gel process, pulsed lazer deposition (PLD), spray pyrolysis and vapor phase deposition [11–14]. Among these methods, sol–gel method can be performed at room temperature, which is advantageous because it is more homogeneous, inexpensive, simple method to control the composition of nano particle and films [15–18]. Nevertheless, the sol–gel nanoparticles and

films have some failures which stem from the processing parameters, drying, heat treatment and annealing condition [19–21]. These failures establish stress based on the difference in the physical and mechanical properties of the elements that connect temperature regime of the product of the nanoparticles. For these reasons, mechanical properties of nanoparticles are investigated to understand stress and to its extent [22–24].

Mechanical properties, including hardness, elastic modulus, yield strength, fracture toughness, brittleness index, and ductility are as important as parameters for industrial applications owing to the useful information on the strength and deformation properties of the materials [25]. Micro-hardness measurements which are performed to obtain the information about the mechanical characteristic of the materials are considered as a significant method to investigate structural parameters [26, 27].

In this study, the development of structural and mechanical properties of ZnO doped with different ratio of Al and Mg is taken as a basis. The ZnO samples doped with Al/Mg were pressed at 4 tons and sintered at a particular temperature. Following this, XRD, SEM and Vickers micro-hardness measurements of these samples were performed, and the effects of Al and Mg doping on

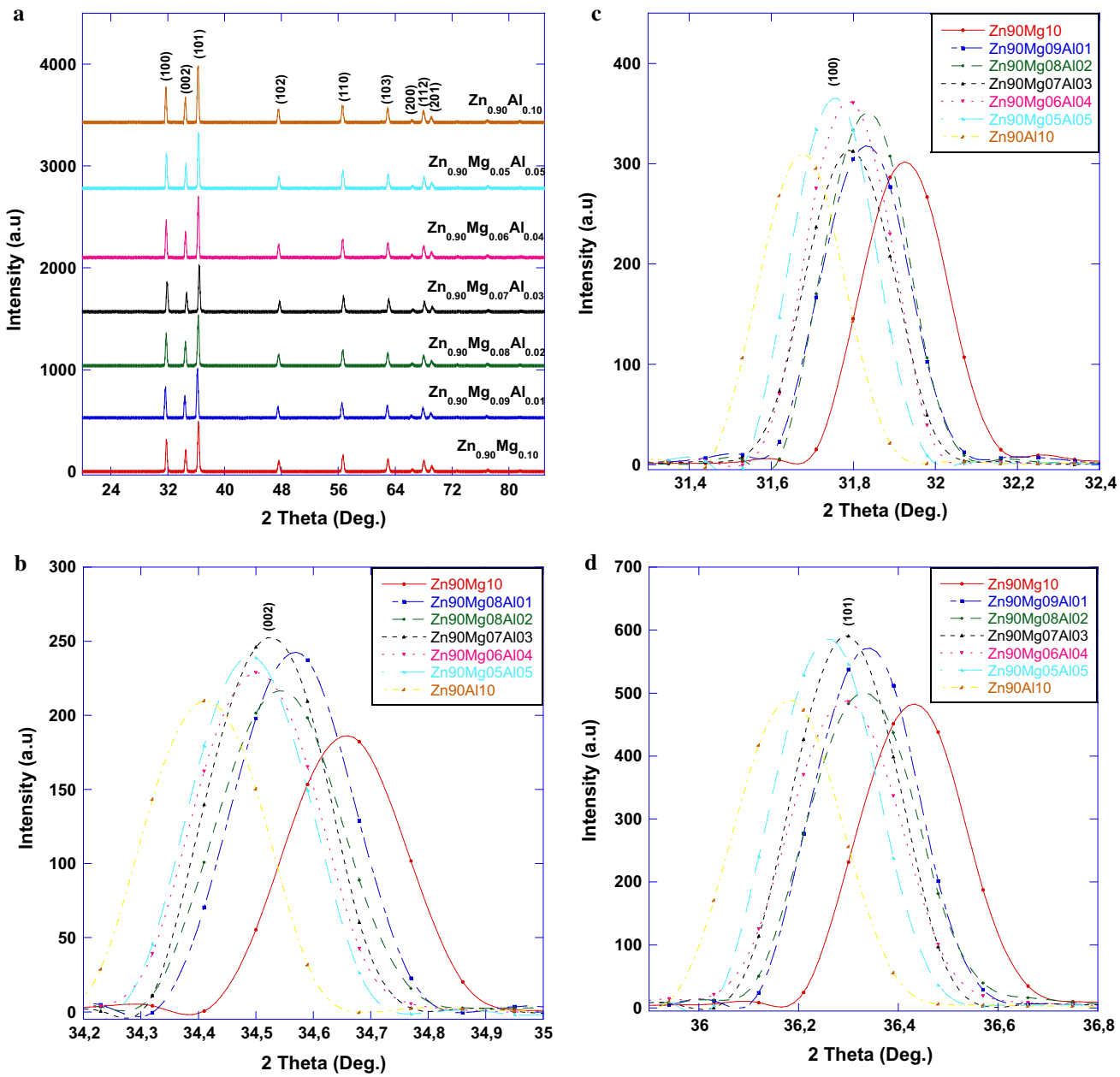


**Fig. 1** **a** XRD patterns of the Al/Mg co-doped ZnO semiconductors, **b–d** Enlarged view of XRD patterns around (002), (100) and (101) peaks

structural and mechanical properties of ZnO were investigated experimentally.

## 2 Experimental procedure

$Zn_{0.90}Mg_{0.10-x}Al_xO$ (ZnMgAlO) system was prepared as polycrystalline nanoparticles with various compositions ($0.0 < x < 0.10$) using sol–gel techniques. Zinc acetate dehydrate, Mg 2, 4 pentadionate, and Al acetylacetonate were used as precursors. Methanol and acetyl acetone were used as a solvent to preparing a homogenous solution. After weighing at appropriate rates, the precursors and solvents were stirred using the magnetic stirrer at room temperature for 8 h until a transparent solution was obtained.

**Table 1** Grains size, *a* and *c* parameters values of undoped and Al-doped samples

| Samples | Grain size (nm) | a (Å) | c (Å) |
|---|---|---|---|
| $Zn_{90}Mg_{10}$ | 41.81 | 3.73 | 5.17 |
| $Zn_{90}Mg_{09}A_{l01}$ | 42.07 | 3.74 | 5.17 |
| $Zn_{90}Mg_{08}A_{l02}$ | 42.35 | 3.74 | 5.17 |
| $Zn_{90}Mg_{07}A_{l03}$ | 42.75 | 3.72 | 5.17 |
| $Zn_{90}Mg_{06}A_{l04}$ | 43.28 | 3.73 | 5.17 |
| $Zn_{90}Mg_{05}A_{l05}$ | 43.50 | 3.74 | 5.16 |
| $Zn_{90}Al_{10}$ | 43.90 | 3.74 | 5.16 |

The ZnMgAlO powders were preheated at 400 °C for 10 min in air and grounded. Grounded nanoparticles were pressed under 4 tons for 5 min into disk shaped compacts with a thickness of 2 mm and a diameter of 10 mm. Pressed samples were annealed at 700 °C for 30 min in air.

The ZnMgAlO phase compositions are characterized by XRD investigation by using a Bruker D8 Advance XRD with $CuK_\alpha$ radiation ($\lambda = 1.5418$ Å) in the range of $2\theta = 20°–80°$ at a scan speed of 1.8°/min and a step increment of 0.09° at room temperature. Phase ratio and lattice parameters *a* and *c* are determined from the XRD patterns. The grain size, grain connectivity and surface morphology of the sample are identified using a Jeol scanning electron microscope (SEM) Quanta FEG 250, operated at 30 kV, with a resolution power of 5 μm. The microhardness analysis of samples was performed using the Vickers microhardness method by a digital static microhardness tester (SHIMADZU) at room temperature. EDS measurements are also made in order to analyze the change

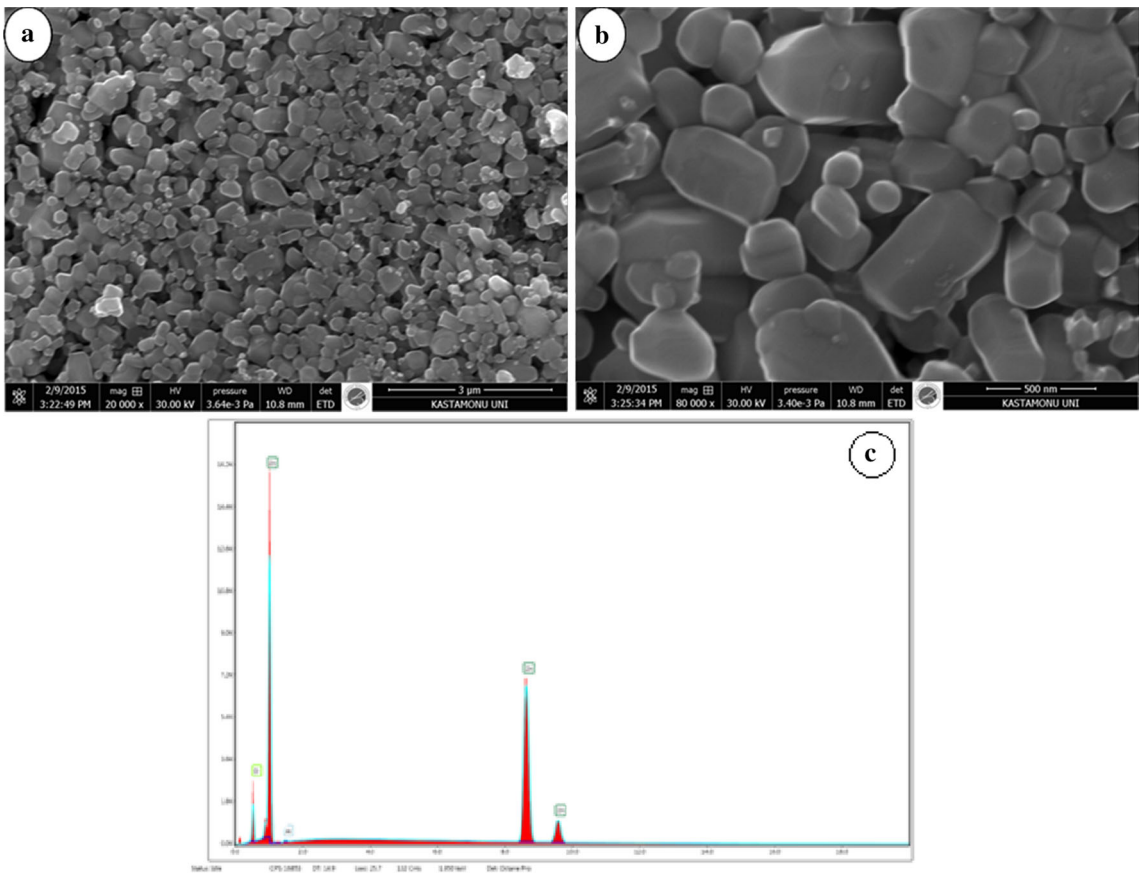


**Fig. 2** **a** and **b** SEM micrographs and **c** EDS of $Zn_{0.90}Al_{0.1}O$ nanoparticles

in the ionic quantity of the samples using the Quanta FEG 250 at 30 kV.

## 3 Result and discussion

### 3.1 XRD and SEM measurements for structural properties

The X-ray diffractions of the $Zn_{0.90}Mg_{0.10-x}Al_xO$ samples are annealed at 700 °C temperatures for 30 min in the air are shown in Fig. 1a. The X-ray analyses show that the reflections correspond to a single phase ZnO with wurtzite hexagonal structure of space group P63mc. *a* and *c* lattice parameters are calculated from XRD peaks using the Eq. 1 and the results are shown in Table 1. As seen from Table 1, a reduction in the *c* lattice parameters observe with increasing the Al concentration.

$$\frac{1}{d^2} = \frac{4^2}{3^2}\frac{(h^2 + hk + k^2)}{a^2} + \frac{l^2}{c^2} \quad (1)$$

The average particle size of $Zn_{0.90}Mg_{0.10-x}Al_xO$ (x = 0.0, 0.01, 0.02, 0.03, 0.04, 0.05 and 0.10) pellet samples are estimated from the data of full width half maximum (FWHM) in the XRD spectrum using the Warren–Sherrer equation Eq. 2. The average particle size is calculated for the highest 5 intense peaks of samples spectrum (100), (002), (101), (110) and (103). Particle sizes of samples are listed in Table 1. From Table 1, particle sizes increase with Al concentration and decrease with Mg concentration.

$$D = \frac{0.941\lambda}{B\cos\theta} \quad (2)$$

$$B^2 = B_s^2 - B_m^2 \quad (3)$$

Enlarged view of XRD patterns around (002) peak in Fig. 1b–d. It is clearly seen that XRD peaks shift to lower angle with the Al addition and intensities change because of the crystallinity and the particle size of the nanoparticles is changed.

SEM images of Al and Mg co-doped ZnO samples are given in Figs. 2, 3, 4, 5, 6, 7 and 8. As seen in the figures, when the Al concentration is increased, the agglomerations of nanoparticles increase. As a result of this the nanoparticles are observed more rectangular form. When the Mg concentration is increased, the nanoparticles are more hexagonal form. Referring to the SEM micrographs almost

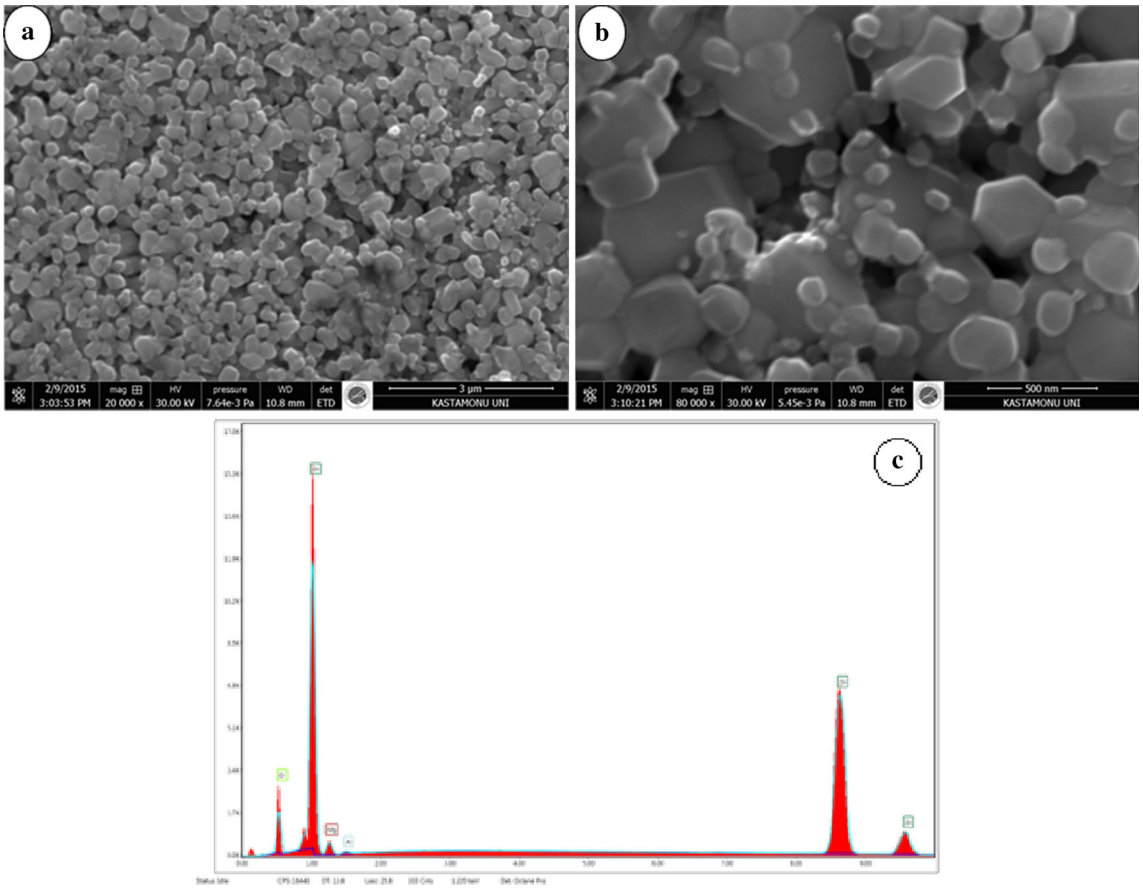


**Fig. 3** **a** and **b** SEM micrographs and **c** EDS of $Zn_{0.90}Mg_{0.05}Al_{0.05}O$ nanoparticles

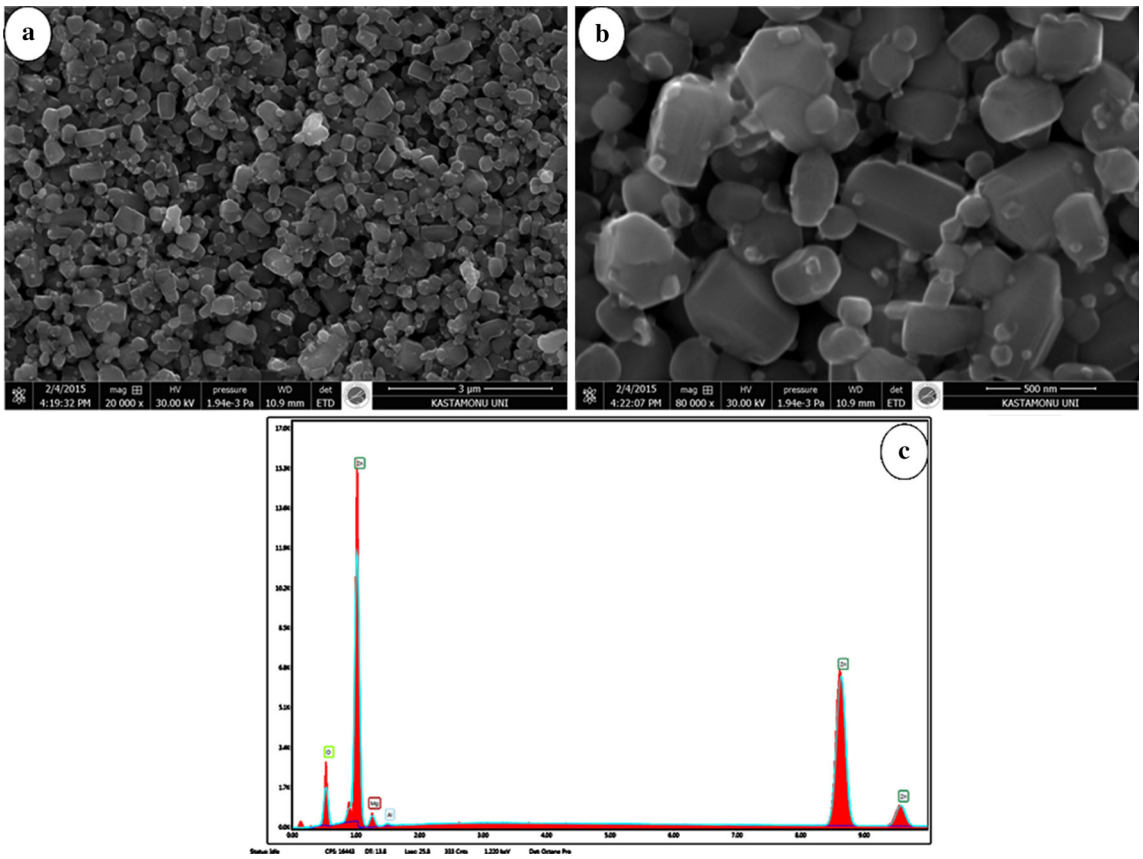


**Fig. 4** **a** and **b** SEM micrographs and **c** EDS of $Zn_{0.90}Mg_{0.06}Al_{0.04}O$ nanoparticles

all nanoparticles are observed hexagonal form for $Zn_{0.90}Mg_{0.1}O$ (without Al concentration) in Fig. 8b. The nanoparticle sizes are observed approximately 100 nm. This result is different from the calculated average particle sizes of the $Zn_{0.90}Mg_{0.10-x}Al_xO$ nanoparticles because of the agglomeration between the nanoparticles due to pressing as is evident from the SEM micrographs.

The composition of $Zn_{0.90}Mg_{0.10-x}Al_xO$ nanoparticles is detected by EDS measurements. EDS results of $Zn_{0.90}Mg_{0.10-x}Al_xO$ (x = 0.00, 0.01, 0.02, 0.03, 0.04, 0.05, and 0.1) nanoparticles are shown in Figs. 2c, 3c, 4c, 5c, 6c, 7c and 8c. Zn, Mg and Al peaks are clearly seen and also Al peaks increase with increasing the Al concentration. Zn, Mg and Al contents of the nanoparticles are the same as those in the preparation of samples.

### 3.2 Vickers microhardness measurements for mechanical characterization

Vickers hardness test was developed to measure the hardness of materials as an alternative to Brinell method [28]. The basic principle, as with all the general principles of hardness, shows the response of material resists to plastic deformation formed with a load applied from a source standard in the material. Vickers test can be used for all materials and have one of the widest scales among hardness tests.

$H_v$ hardness is determined by *F/A* ratio. *F* is applied load on the surface of material. *A* is surface area in the terms of micrometers square. *A* can be calculated by the following formula:

$$A = \frac{l^2}{2\sin(136^\circ/2)} \tag{4}$$

$$A \approx \frac{l^2}{1854.4} \tag{5}$$

The Vickers microhardness values ($H_v$) of different applied loadings in the range of 0.245–2.940 N for 10 s can be calculated using Eq. 6. This process is repeated 7 times and the average value of hardness is found. The values given in the Table 2 and Fig. 9 are the average values of Vickers microhardness.

$$H_v = F/A \approx \frac{1854.4F}{l^2} \quad \text{GPa} \tag{6}$$

It can be seen from Fig. 9 that the microhardness values decrease with increasing both the *Al* doping level and applied load. Microhardness values have reached the

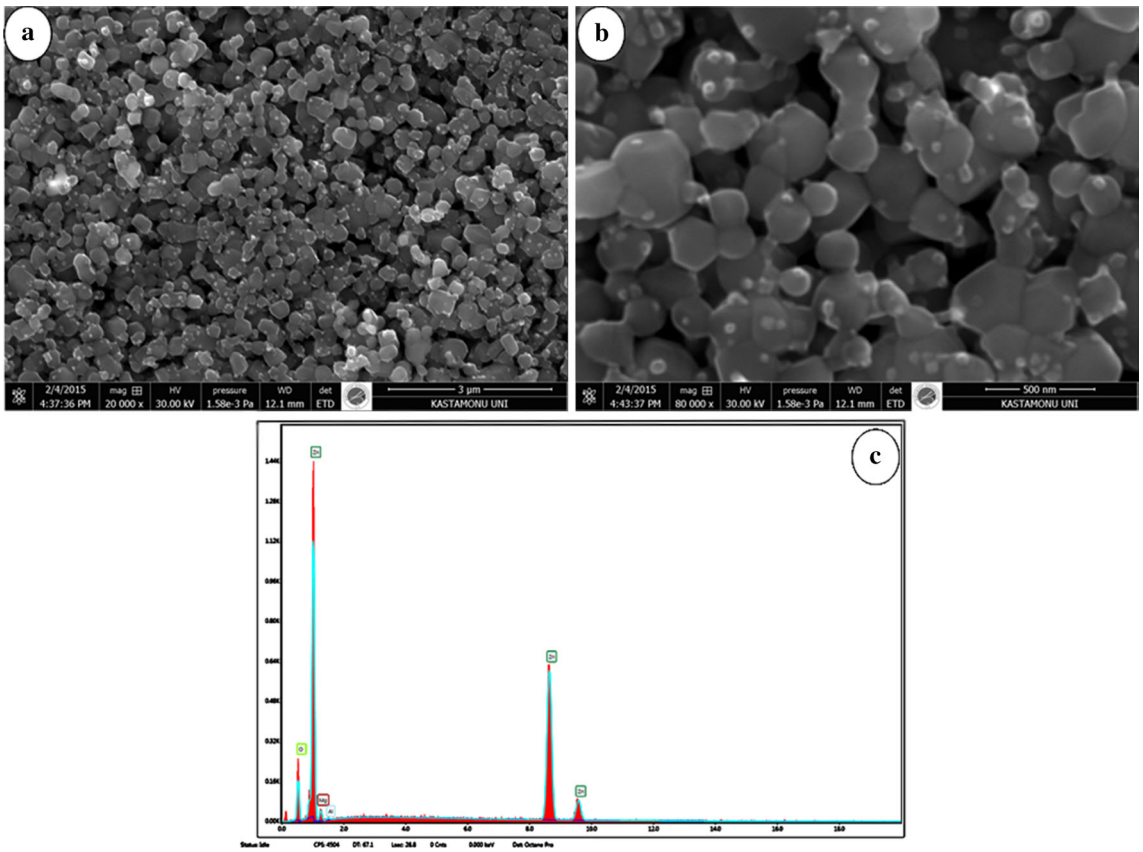


**Fig. 5** **a** and **b** SEM micrographs and **c** EDS of $Zn_{0.90}Mg_{0.07}Al_{0.03}O$ nanoparticles

plateau (saturation region) around about 1.5 *N* for the samples.

The hardness value of the sample observe *ISE* behavior depends on the applied load. It shows that the indenter size is associated with applied load. This nonlinear case is named as Indentation Size Effect (ISE) in the literature [29, 30]. Smaller indentation load shows a greater hardness value. This observation is relevant to the being weak grain boundaries of materials.

Parameters such as modulus of elasticity (E), brittleness ($B_i$), fracture toughness ($K_{IC}$), yield strength (Y) and ductility (D) that are as important as hardness to mechanical characterizations of materials are also calculated and values of these parameters are given in Table 2.

### 3.2.1 *Description of mechanical parameters*

The modulus of elasticity (E) is a measure of elastic deformation of the material under force. In some sources, it is also referred to as Young's modulus and calculated as described below. Materials become more rigid with increasing the *E*. In order words, material shows less deformation with strain. When elasticity modulus (E) is small the material acts more flexible/elastic.

$$E = 81.9635H_V \tag{7}$$

Brittleness ($B_i$) is the tendency of a material has undergone very little fracture or has no deformation that is pre-determined to fracture in technical using. It means that material doesn't have the ability to plastic deformation. Brittleness ($B_i$) is the opposite ductility (D). Ductility is the ability of a material to permanent deformation.

$$B_i = H_v/K_{IC} \tag{8}$$

$$D = 1/B_i \tag{9}$$

Toughness of the material is a maximum amount of energy is absorbed before fracture. At the same time, it is described as plastic deformation capability of the material. Because elastic and plastic deformation allow for absorption of a majority of energy by the material, toughness can be small in brittle materials. In materials science, fracture toughness is a property that defines the ability of the material which contains cracks formed by fracture. It is one of the important features of any material in many design applications. Linear elastic fracture toughness of a material was determined by the formation of a crack that begins to grow in the material. It is shown as $K_{IC}$ and its unit is $Pa\sqrt{m}$ or $psi\sqrt{in}$.

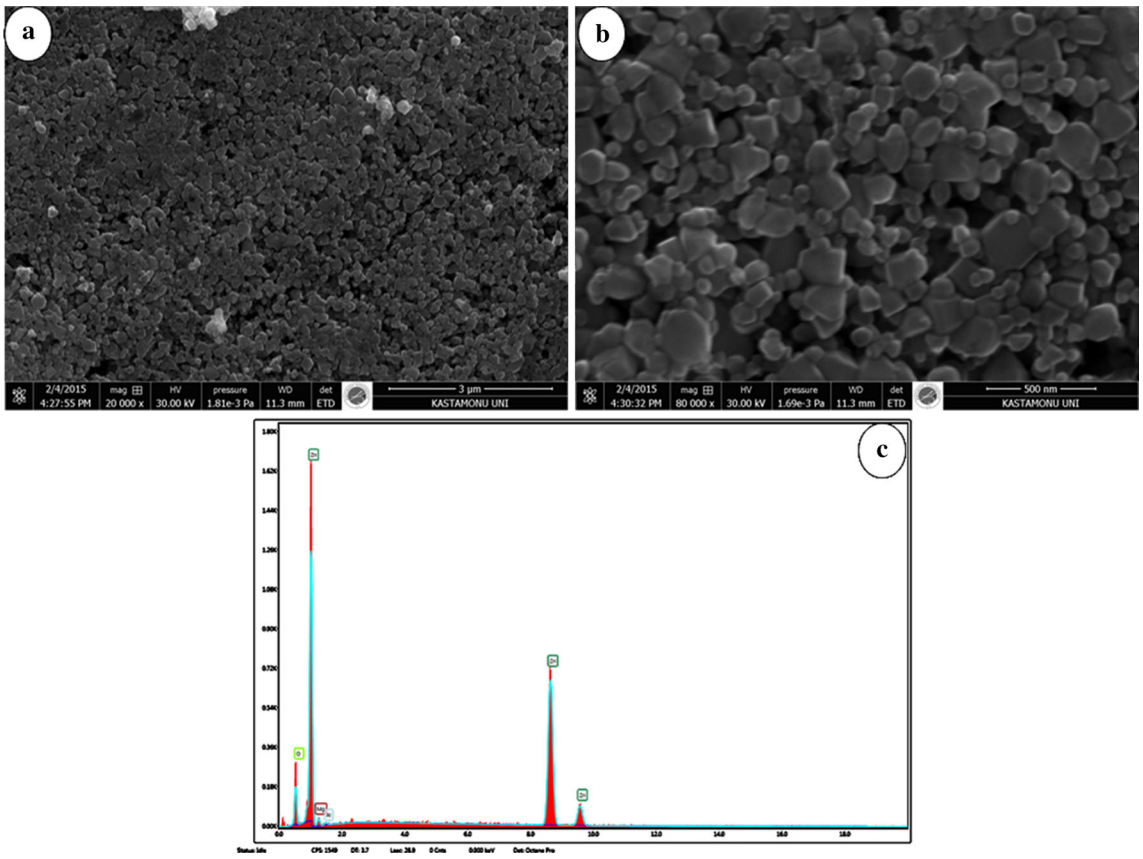


**Fig. 6** **a** and **b** SEM micrographs and **c** EDS of $Zn_{0.90}Mg_{0.08}Al_{0.02}O$ nanoparticles

$$K_{IC} = \sqrt{2E\gamma} \tag{10}$$

Yield strength (Y) represents transition point from elastic deformation to plastic deformation.

$$Y \approx H_V/3 \tag{11}$$

As seen from Table 2, $E$, $Y$, $B_i$ and $D$ values decrease owing to the relation of the hardness. Decrease of the $K_{IC}$ value is an expected result due to dependency of $E$.

More detailed analysis is made using data obtained from all results regarding microhardness of materials that have *ISE* behavior. Therefore, the different models are presented in order to explain the *ISE* behavior in the literature [31–33]. In this section, the comparisons are relevant to hardness will be made using the Meyer's Law, the *PSR*, the *EPD* model and the *HK* approach. Analyses on these models are given below.

### 3.2.2 *Meyer's law is used to determination of material behavior*

Meyer's law which is an expression of simple experimental developed to explain of *ISE* (Indentation Size Effect) or *RISE* (Reverse Indentation Size Effect) behavior of materials [34] (Fig. 10).

$$F = Kl^n \tag{12}$$

Meyer number $n$ is a measure of *ISE or RISE*. If the $n$ value is greater than *2*, RISE behavior is obtained, If the $n$ value is less than *2*, *ISE* behavior is obtained [35–37]. According to results of Meyer's Law, all samples show *ISE* behavior (Table 3).

### 3.2.3 *Proportional sample resistance (PSR) model*

In this model, it is expressed that sample resistance is not constant and increases with indentation depth like in Hays Kendall approach Eq. 13 (Fig. 11).

$$F/l = \alpha + \beta l \tag{13}$$

From Table 4 it is seen that the value of $\alpha$ is positive for all samples. This result shows that there is elastic deformation in the samples along with plastic deformation.

Quinn and Quinn [35] show that there is a transition region to plateau where hardness remains unchanged after from a certain of load value in hardness-load change curves [35]. They denoted that the hardness value corresponds to hardness in this region is called as the plateau regions true hardness. When $H_v$ values of produced ZnMgAlO semiconductors are analyzed

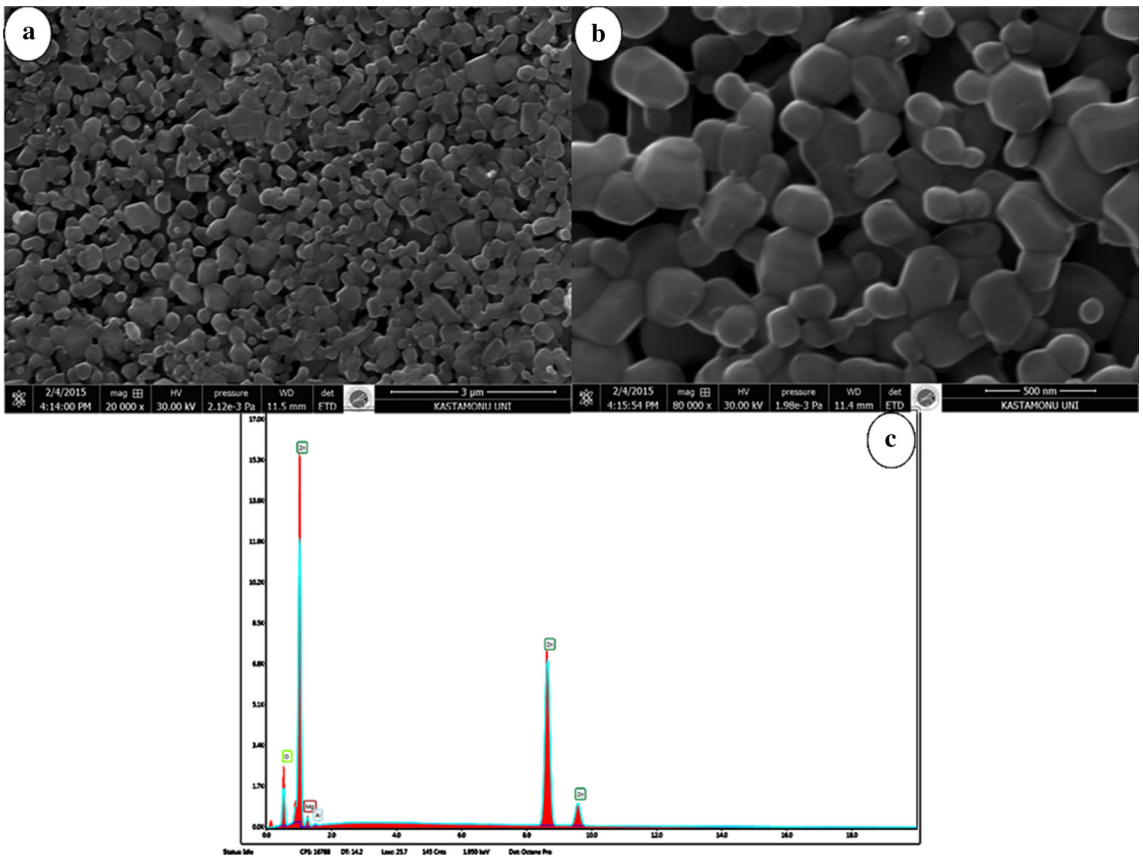


**Fig. 7** **a** and **b** SEM micrographs and **c** EDS of $Zn_{0.90}Mg_{0.09}Al_{0.01}O$ nanoparticles

(Table 2), it is observed that hardness reaches to plateau region after 1.5 *N*. If $H_{PSR}$ hardness values are compared with value that corresponds to the plateau region, it can be seen clearly that these microhardness values are quite far from the plateau region. Therefore, this model is not sufficient for determination of true hardness.

### 3.2.4 Elastic/plastic deformation (EPD) model

In the most of the indentation tests, the size of indentation is measured after indenter is removed from sample surface. Elastic recovery is observed around of indentation trace forms after indenter is removed. So that, the indentation size decreases until a certain value. Taking into account this condition, the addition of a new term to measured indentation size is deemed appropriate for calculation the load independent hardness [38, 39]. According to this result, hardness in the *EDP* model,

$$F^{1/2} = A_1^{1/2} l_p + A_2^{1/2} l_e \tag{14}$$

is given by Eq. 14 (Fig. 12).

As seen from Table 5, the value of $l_e$ is positive for all samples. That means, elastic deformation is observed along with plastic deformation for this range of applied loads. For all samples elastic recovery is present. Presence of elastic deformation along with plastic deformation is the reason of *ISE* behavior for our samples. As a result, this model is not sufficient for determination of true hardness.

### 3.2.5 Hays–Kendall (HK) approach

Hays and Kendall suggested that minimum load value (W) can create permanent deformation in a sample. If the applied load does not exceed this resistance, permanent deformation does not occur and only elastic deformation occurs. So, a test load may be generated only elastic deformation under a certain limit value and both elastic and plastic deformation above this critical value [40]. According to *HK* approach, effective load $F_{eff} = F - W_{HK}$ is used instead of applied load *F*.

$$F - W_{HK} = A_{HK} d^2 \tag{15}$$

As can be seen from *F* versus $d^2$ graph (Fig. 13), the curves are linear for all samples. In Table 6, the values of $W_{HK}$, $A_{1HK}$ and the $H_{HK}$ values are tabulated. The values of $W_{HK}$ are positive for all samples which can be interpreted

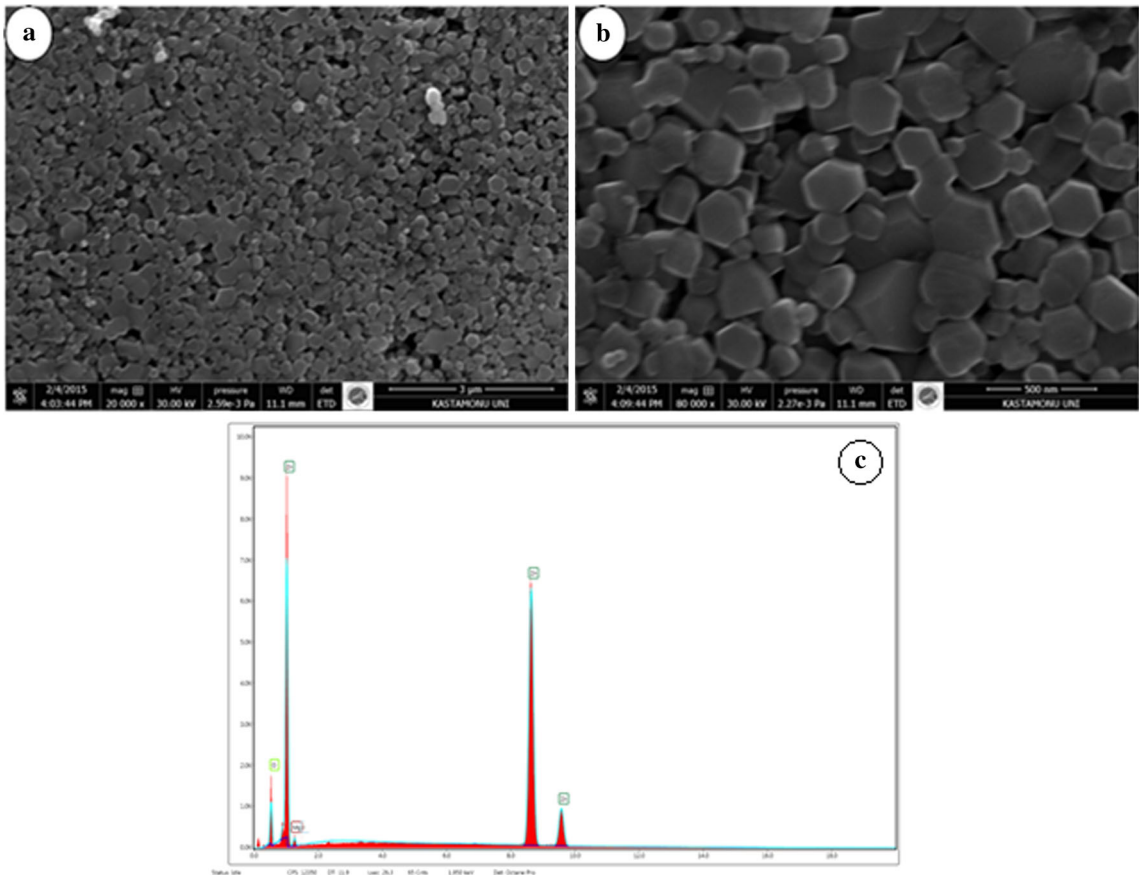


**Fig. 8** **a** and **b** SEM micrographs and **c** EDS of $Zn_{0.90}Mg_{0.1}O$ nanoparticles

**Table 2** The load dependent $H_v$, $E$, $Y$, $K_{IC}$, $B_i$ and $D$ for the samples

| Samples | $H_v$ (GPa) | E (GPa) | Y (GPa) | $K_{IC} \times 10^3$ (Pa/m$^{1/2}$) | $B_i \times 10^4$ (m$^{1/2}$) | D (m$^{-1/2}$) |
|---|---|---|---|---|---|---|
| $Zn_{90}Mg_{10}$ | 1.113 | 91.22 | 0.371 | 845.67 | 131.61 | 75.98 |
| | 1.025 | 84.01 | 0.341 | 811.57 | 126.30 | 79.17 |
| | 0.906 | 74.25 | 0.302 | 762.97 | 118.75 | 84.21 |
| | 0.862 | 70.65 | 0.287 | 744.24 | 115.82 | 86.33 |
| | 0.855 | 70.07 | 0.285 | 741.18 | 115.36 | 86.68 |
| $Zn_{90}Mg_{09}A_{l01}$ | 1.027 | 84.17 | 0.342 | 730.51 | 140.59 | 71.13 |
| | 0.958 | 78.52 | 0.319 | 705.56 | 135.78 | 73.64 |
| | 0.841 | 68.93 | 0.280 | 661.07 | 127.22 | 78.60 |
| | 0.826 | 67.70 | 0.275 | 655.15 | 126.08 | 79.31 |
| | 0.820 | 67.21 | 0.273 | 652.77 | 125.62 | 79.60 |
| $Zn_{90}Mg_{08}A_{l02}$ | 0.809 | 66.30 | 0.269 | 845.41 | 95.69 | 104.50 |
| | 0.564 | 46.22 | 0.188 | 705.87 | 79.90 | 125.15 |
| | 0.466 | 38.19 | 0.155 | 641.63 | 72.62 | 137.69 |
| | 0.438 | 35.90 | 0.146 | 622.09 | 70.40 | 142.03 |
| | 0.425 | 34.83 | 0.141 | 612.75 | 69.35 | 144.18 |
| $Zn_{90}Mg_{07}A_{l03}$ | 0.768 | 62.94 | 0.256 | 778.94 | 98.59 | 101.42 |
| | 0.514 | 42.12 | 0.171 | 637.21 | 80.66 | 123.97 |
| | 0.435 | 35.65 | 0.145 | 586.23 | 74.20 | 134.77 |

**Table 2** continued

| Samples | $H_v$ (GPa) | E (GPa) | Y (GPa) | $K_{IC} \times 10^3$ (Pa/m$^{1/2}$) | $B_i \times 10^4$ (m$^{1/2}$) | D (m$^{-1/2}$) |
|---|---|---|---|---|---|---|
| | 0.420 | 34.42 | 0.140 | 576.03 | 72.91 | 137.15 |
| | 0.412 | 33.76 | 0.137 | 570.48 | 72.22 | 138.47 |
| $Zn_{90}Mg_{06}A_{l04}$ | 0.684 | 56.06 | 0.228 | 695.15 | 98.39 | 101.63 |
| | 0.454 | 37.21 | 0.151 | 566.35 | 80.16 | 124.75 |
| | 0.400 | 32.78 | 0.133 | 531.57 | 75.24 | 132.89 |
| | 0.382 | 31.31 | 0.127 | 519.51 | 73.53 | 136.00 |
| | 0.378 | 30.98 | 0.126 | 516.77 | 73.14 | 136.71 |
| $Zn_{90}Mg_{05}A_{l05}$ | 0.660 | 54.09 | 0.220 | 660.28 | 99.95 | 100.04 |
| | 0.383 | 31.39 | 0.127 | 502.99 | 76.14 | 131.33 |
| | 0.365 | 29.91 | 0.121 | 490.99 | 74.34 | 134.52 |
| | 0.352 | 28.85 | 0.117 | 482.21 | 72.99 | 136.99 |
| | 0.346 | 28.35 | 0.115 | 478.02 | 72.38 | 138.16 |
| $Zn_{90}A_{l10}$ | 0.580 | 47.53 | 0.193 | 614.32 | 94.41 | 105.92 |
| | 0.366 | 29.99 | 0.122 | 487.98 | 75.00 | 133.33 |
| | 0.330 | 27.04 | 0.110 | 463.35 | 71.22 | 140.41 |
| | 0.320 | 26.22 | 0.106 | 456.27 | 70.13 | 142.58 |
| | 0.310 | 25.40 | 0.103 | 449.08 | 69.03 | 144.86 |

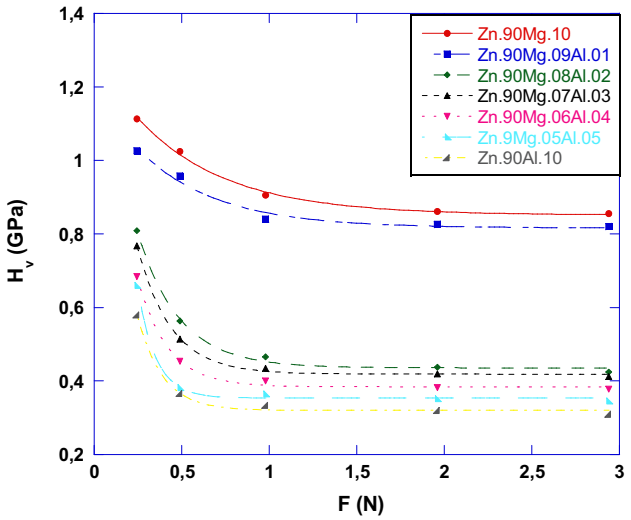


**Fig. 9** Vickers microindentation hardness variation as a function of indentation test load for all samples

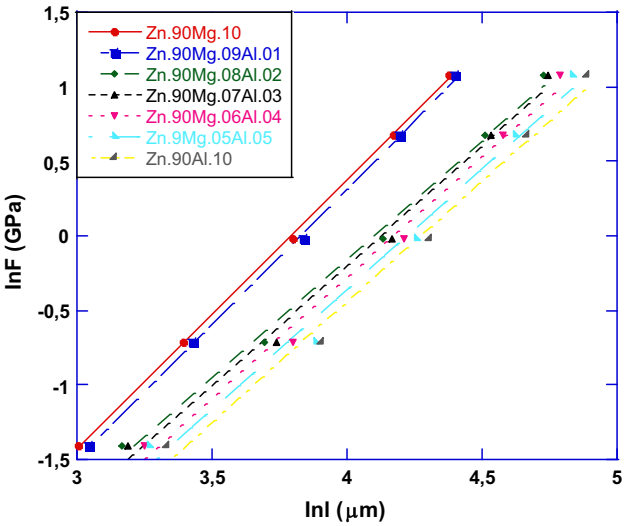


**Fig. 10** Variation of *lnF* with *lnl* for all samples

as the applied load is enough to create both the elastic and plastic deformation [41, 42]. Among these models, the values of microhardness calculated using *HK* model are the closest to the values of the plateau (saturation) region (Table 7).

For comparative analysis of the all applied models, the hardness value of each model is given in Table 7. It can be seen clearly that the most appropriate model is *HK* approach for the all samples which are showed *ISE* behavior.

## 4 Conclusion

The effects of Al and Mg doping on the structural and mechanical properties are investigated by using X-Ray diffraction, scanning electron microscopy and digital micro-hardness tester. According to the XRD measurements, all samples have wurtzite hexagonal structure of ZnO. A reduction in the *c* lattice parameters observe and the XRD peaks shift to lower angle with increasing the Al concentration. By using the SEM images, it is observed that when the Al concentration is increased, the

**Table 3** Regression analysis of experimental data according to Meyer's law

| Samples | n | InK (GPa) |
|---|---|---|
| $Zn_{90}Mg_{10}$ | 1.79 | −6.81 |
| $Zn_{90}Mg_{09}A_{l01}$ | 1.82 | −6.97 |
| $Zn_{90}Mg_{098}A_{l02}$ | 1.59 | −6.53 |
| $Zn_{90}Mg_{07}A_{l03}$ | 1.60 | −6.63 |
| $Zn_{90}Mg_{06}A_{l04}$ | 1.62 | −6.78 |
| $Zn_{90}Mg_{05}A_{l05}$ | 1.61 | −6.79 |
| $Zn_{90}A_{l10}$ | 1.61 | −6.90 |

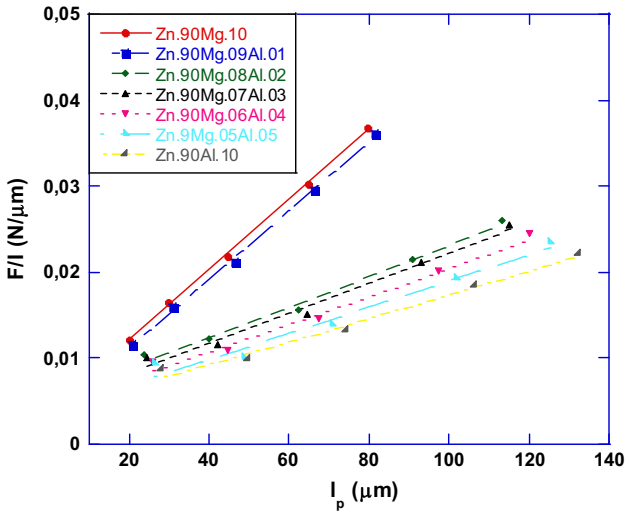


**Fig. 11** Plots of *F/l* versus *l* for the samples

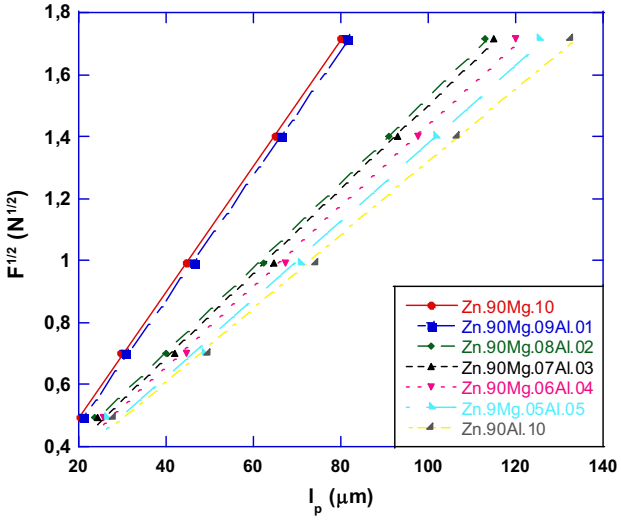


**Fig. 12** Plots of $F^{1/2}$ versus $l_p$ for the samples

**Table 5** Regression analysis of experimental data according to *EPD* model

| Samples | $l_e$ (μm) | $A_2^{1/2}$ (GPa) | $H_{EPD}$ (GPa) | $H_v$ (GPa) |
|---|---|---|---|---|
| $Zn_{90}Mg_{10}$ | 0.086 | 0.020 | 0.741 | 0.862–0.855 |
| $Zn_{90}Mg_{09}A_{l01}$ | 0.071 | 0.020 | 0.741 | 0.8←26–0.820 |
| $Zn_{90}Mg_{08}A_{l02}$ | 0.155 | 0.013 | 0.313 | 0.438–0.425 |
| $Zn_{90}Mg_{07}A_{l03}$ | 0.141 | 0.013 | 0.313 | 0.420–0.412 |
| $Zn_{90}Mg_{06}A_{l04}$ | 0.133 | 0.013 | 0.313 | 0.382–0.378 |
| $Zn_{90}Mg_{05}A_{l05}$ | 0.126 | 0.012 | 0.267 | 0.352–0.346 |
| $Zn_{90}A_{l10}$ | 0.133 | 0.011 | 0.224 | 0.320–0.310 |

agglomerations of nanoparticles increase. The nanoparticles are observed more rectangular form. When the Mg concentration is increased, the nanoparticles are more hexagonal form. The obtained experimental microhardness results were analyzed by using Meyer's law, proportional specimen resistance (PSR) model, elastic/plastic deformation (EPD) model, and Hays–Kendall (HK) approach available in the literature. Among these model Hays-Kendall model is more suitable to determine the micromechanical properties of the Al/Mg co-doped ZnO nanoparticles showed ISE behavior.

The Vickers microhardness values ($H_v$) were decreased with increasing the Al concentration and the applied load. The load-dependent elastic modulus, yield strength, fracture toughness, brittleness and ductility were calculated. It is found that these values decreased with increasing Al concentration.

**Table 4** Regression analysis of experimental data according to *PSR* model

| Samples | $\alpha \times 10^{-3}$ (N) | $\beta \times 10^{-5}$ (N/μm) | $H_{PSR}$ (GPa) | $H_V$ (GPa) |
|---|---|---|---|---|
| $Zn_{90}Mg_{10}$ | 3.92 | 40.84 | 0.757 | 0.862–0.855 |
| $Zn_{90}Mg_{09}A_{l01}$ | 3.17 | 39.96 | 0.741 | 0.826–0.820 |
| $Zn_{90}Mg_{08}A_{l02}$ | 5.39 | 17.78 | 0.329 | 0.438–0.425 |
| $Zn_{90}Mg_{07}A_{l03}$ | 4.82 | 17.51 | 0.324 | 0.420–0.412 |
| $Zn_{90}Mg_{06}A_{l04}$ | 4.31 | 16.31 | 0.302 | 0.382–0.378 |
| $Zn_{90}Mg_{05}A_{l05}$ | 4.03 | 15.00 | 0.278 | 0.352–0.346 |
| $Zn_{90}Al10$ | 3.97 | 13.41 | 0.248 | 0.320–0.310 |

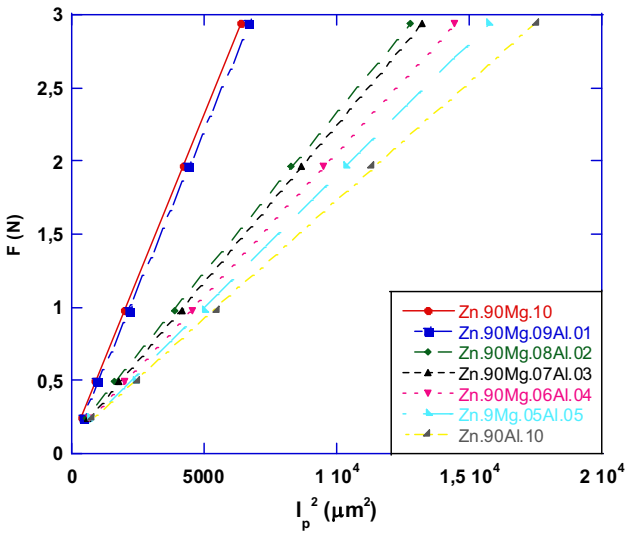


**Fig. 13** Plots of F versus $l_p^2$ for the samples

**Table 6** Regression analysis of experimental data according to *HK* model

| Samples | $A_{HK} \times 10^{-5}$ | $W_{HK}$ (N) | $H_{HK}$ (GPa) | $H_V$ (GPa) |
|---|---|---|---|---|
| $Zn_{90}Mg_{10}$ | 44.86 | 0.076 | 0.831 | 0.862–0.855 |
| $Zn_{90}Mg9A_{l01}$ | 43.28 | 0.059 | 0.802 | 0.826–0.820 |
| $Zn_{90}Mg_{08}A_{l02}$ | 21.99 | 0.127 | 0.407 | 0.438–0.425 |
| $Zn_{90}Mg_{07}A_{l03}$ | 21.37 | 0.108 | 0.396 | 0.420–0.412 |
| $Zn_{90}Mg_{06}A_{l04}$ | 19.62 | 0.100 | 0.363 | 0.382–0.378 |
| $Zn_{90}Mg_{05}A_{l05}$ | 18.10 | 0.088 | 0.335 | 0.352–0.346 |
| $Zn_{90}A_{l10}$ | 16.17 | 0.103 | 0.299 | 0.320–0.310 |

**Table 7** The results of load dependent Vickers microhardness at the plateau region and load independent hardness values calculated using *PSR*, *EPD* and *HK* models

| Samples | $H_V$ (GPa) (in plateauregion) | $H_{PSR}$ (GPa) | $H_{EPD}$ (GPa) | $H_{HK}$ (GPa) |
|---|---|---|---|---|
| Zn90Mg10 | 0.862–0.855 | 0.757 | 0.741 | 0.831 |
| $Zn_{90}Mg_{09}A_{l01}$ | 0.826–0.820 | 0.741 | 0.741 | 0.802 |
| $Zn_{90}Mg_{08}A_{l02}$ | 0.438–0.425 | 0.329 | 0.313 | 0.407 |
| $Zn_{90}Mg_{07}A_{l03}$ | 0.420–0.412 | 0.324 | 0.313 | 0.396 |
| $Zn_{90}Mg_{06}A_{l04}$ | 0.382–0.378 | 0.302 | 0.313 | 0.363 |
| $Zn_{90}Mg_{05}A_{l05}$ | 0.352–0.346 | 0.278 | 0.267 | 0.335 |
| $Zn_{90}A_{l10}$ | 0.320–0.310 | 0.248 | 0.224 | 0.299 |

**Acknowledgments** This research has been supported by the Kastamonu University Scientific Research Projects Coordination Department under the Grant No. KUBAP-03/2013-41, the Abant İzzet Baysal University Scientific Research Projects Coordination Department under the Project No: 2014.03.03.723 and the Scientific and Technological Research Council of Turkey (TÜBİTAK) Project No. 114F259.

**Compliance with Ethical Standards**

**Conflict of interest** The authors declares that there is no conflict of interests regarding the publication of this article.

## References

1. S. Jeong, J. Park, B. Teak Lee, J. Alloys Compd. **617**, 180–184 (2014)
2. Z. Pan, X. Tian, S. Wu, C. Xiao, Z. Li, J. Deng, G. Hu, Z. Wei, Super. Nicrostr. **54**, 107–117 (2013)
3. G. Claes, Granqvist. Thin Solid Films **564**, 1–38 (2014)
4. R.A. Ismail, B.G. Rasheed, E.T. Salm, M. Al-Hadethy, J. Mater. Sci. Mater. Electron. **18**, 397–400 (2007)
5. O. Baka, A. Azizi, S. Velumani, G. Schmerber, A. Dinia, J. Mater. Sci. Mater. Electron. **25**, 1761–1769 (2014)
6. U. Ozgur, Y. Alivov, C.Y.I. Liu, A. Teke, M. Reshchikov, S. Doğan, A. Avrutin, V.S.-J. Cho, H. Morkoc, J. Appl. Phys. **98**, 041301 (2005)
7. N. Kilinc, S. Ozturk, L. Arda, A. Altindal, Z.Z. Ozturk, J. Alloy. Compd. **536**, 138–144 (2012)
8. L. Arda, M. Acikgoz, N. Dogan, D. Akcan, O. Cakiroglu, J. Supercond. Nov. Magn. **27**, 799–804 (2013)
9. N. Kilinc, L. Arda, S. Ozturk, Z.Z. Ozturk, Cryst. Res. Technol. **45**, 529–538 (2010)
10. Z.K. Heiba, L. Arda, M.B. Mohamed, N.Y. Mostafa, M.A. Al-Jalali, N. Dogan, J. Supercond. Nov. Magn. **26**, 3299–3304 (2013)
11. L. Arda, M. Acikgoz, Z.K. Heiba, N. Dogan, D. Akcan, O. Cakiroglu, Solid State Commun. **170**, 14–18 (2013)
12. J. Meyer, P. Görrn, S. Hamwi, H.H. Johannes, T. Riedl, W. Kowalsky, Appl. Phys. Lett. **93**, 073308 (2008)
13. N.S. Kumar, K.V. Bangera, G.K. Shivakumar, Semiconductors **48**, 1023–1027 (2014)
14. J. Huang, R. Tan, Y. Zhang, J. Li, Y. Yang, X. Zhang, W. Song, J. Mater. Sci. Mater. Electron. **23**, 356–360 (2012)
15. Z.K. Heiba, L. Arda, J. Mol. Struct. **1022**, 167–171 (2012)
16. Z.K. Heiba, L. Arda, Cryst. Res. Technol. **44**, 845–850 (2009)
17. L. Arda, M. Acikgoz, A. Gungor, J. Supercond. Nov. Magn. **25**, 2701–2705 (2012)
18. O. Cakiroglu, M. Acikgoz, L. Arda, D. Akcan, N. Dogan, J. Magn. Mater. **373**, 60 (2015)
19. L. Arda, S. Ataoglu, J. Alloy. Compd. **471**, 282–290 (2009)
20. L. Arda, S. Ataoglu, Z. Abdulaliyev, O.A. Sacli, J. Alloy. Compd. **470**, 404–407 (2009)
21. L. Arda, S. Ataoglu, S. Sezer, Z. Abdulaliyev, Surf. Coat. Technol. **202**, 439–446 (2007)
22. M. Tosun, S. Ataoglu, L. Arda, O. Ozturk, E. Asikuzun, D. Akcan, O. Cakiroglu, Mater. Sci. Eng., A **590**, 416–422 (2014)
23. E. Asikuzun, A. Donmez, L. Arda, O. Cakiroglu, D. Akcan, O. Ozturk, M. Tosun, S. Ataoglu, C. Terzioglu, Ceram. Int. **41**, 6326–6334 (2015)
24. L. Arda, O. Ozturk, E. Asikuzun, S. Ataoglu, Powder Technol. **235**, 479–484 (2013)
25. M. Yilmazlar, O. Ozturk, O. Gorur, I. Belenli, C. Terzioglu, Supercond. Sci. Technol. **20**, 365–371 (2007)
26. E. Asikuzun, O. Ozturk, H.A. Cetinkara, G. Yildirim, A. Varilci, M. Yılmazlar, C. Terzioglu, J. Mater. Sci. Mater. Electron. **23**, 1001–1010 (2012)
27. H. Aydın, A. Babanli, S.P. Altintas, E. Asikuzun, N. Soylu, O. Ozturk, M. Dogruer, C. Terzioglu, G. Yildirim, J. Mater. Sci. Mater. Electron. **24**, 4566–4573 (2013)
28. R.L. Smith, G.E. Sandland, Proc. Inst. Mech. Eng. **1**, 623–641 (1922)

29. J. Gong, J. Wu, Z. Guan, J. Eur. Ceram. Soc. **19**, 2625–2631 (1999)
30. A.A. Elmustafa, D.S. Stone, J. Mech. Phys. Solids **51**, 357–381 (2003)
31. U. Kölemen, O. Uzun, M. Yilmazlar, E. Yanmaz, J. Alloys Compd. **145**, 300–306 (2006)
32. O. Sahin, O. Uzun, M. Sopicka-Lizer, H. Gocmez, U. Kölemen, J. Eur. Ceram. Soc. **28**, 1235–1242 (2008)
33. O. Ozturk, H.A. Cetinkara, E. Asıkuzun, M. Akdogan, M. Yilmazlar, C. Terzioglu, J. Mater. Sci. Mater. Electron. **22**, 1501–1508 (2011)
34. R. Awad, A.I. Abou-Aly, M. Kamal, M. Anas, J. Supercond. Nov. Magn. **24**, 1947–1956 (2011)
35. J.B. Quinn, V.D. Quinn, J. Sci. **32**, 4331–4346 (1997)
36. H.A. Cetinkara, M. Yilmazlar, O. Ozturk, M. Nursoy, C. Terzioglu, J. Phys: Conf. Ser. **153**, 012038 (2009)
37. O. Ozturk, M. Erdem, E. Asikuzun, O. Yildiz, G. Yildirim, A. Varilci, C. Terzioglu, J. Mater. Sci. Mater. Electron. **24**, 230–238 (2013)
38. G.P. Upit, S.A. Varchenya, Phys. Status Solidi A **17**, 831 (1966)
39. S.J. Bull, T.F. Page, E.H. Yoffe, Philos. Mag. Lett. **59**, 281 (1989)
40. C. Hays, E.G. Kendall, Metallography **6**, 275–282 (1973)
41. O. Ozturk, E. Asikuzun, S. Kaya, G. Yildirim, M.B. Turkoz, A. Kilic, J. Sup. Nov. Magn. **27**, 1403–1412 (2014)
42. S. Safran, A. Kılıç, E. Asikuzun, E. Kılıçarslan, O. Ozturk, A. Gencer, J. Mater. Sci. Mater. Electron. **25**, 2737–2747 (2014)